

Taylor-Couette flow with split endcaps: preparatory hydrodynamic study for upcoming DRESDYN-MRI experiment

Ashish Mishra*

*Helmholtz-Zentrum Dresden-Rossendorf, Bautzner Landstr. 400, D-01328 Dresden, Germany and
Center for Astronomy and Astrophysics, TU Berlin, Hardenbergstr. 36, 10623 Berlin, Germany*

Paolo Personnettaz

Université Grenoble Alpes, CNRS, ISTERre, 38000 Grenoble, France

George Mamatsashvili

*Helmholtz-Zentrum Dresden-Rossendorf, Bautzner Landstr. 400, D-01328 Dresden, Germany and
Abastumani Astrophysical Observatory, Abastumani 0301, Georgia*

Vladimir Galindo and Frank Stefani

Helmholtz-Zentrum Dresden-Rossendorf, Bautzner Landstr. 400, D-01328 Dresden, Germany

Magnetorotational instability (MRI) is of great importance in astrophysical disks, driving angular momentum transport and accretion of matter onto a central object. A Taylor-Couette (TC) flow between two coaxial cylinders subject to an axial magnetic field is a preferred setup for MRI-experiments. A main challenge in those experiments has been to minimize the effects of axial boundaries, or endcaps, which substantially alter the flow structure compared to the axially unbounded idealized case. Understanding the influence of endcaps on the flow stability is crucial for the unambiguous experimental identification of MRI. In this paper, we examine the hydrodynamic evolution of a TC flow in the presence of split endcap rims up to Reynolds number $Re = 2 \times 10^5$. At this Re , the flow deviates from the ideal TC flow profile, resulting in about 15% deviation in angular velocity at the mid-height of the cylinders. Aside from turbulent fluctuations caused by shearing instability at the endcaps, the bulk flow remains axially independent and exhibits Rayleigh stability. We characterize the scaling of the Ekman and Stewartson boundary layer thickness with respect to Re . We also study the effect of changing the rotation ratio of the cylinders μ on the flow at large Re and show that TC experiments can be conducted for larger $\mu \sim 0.5$ to safely ensure the hydrodynamic stability of the flow in the upcoming DRESDYN-MRI experiment. In all configurations considered, the modification of the flow profile by the endcaps further decreases the required critical threshold for the onset of MRI that can facilitate its detection in future experiments.

I. INTRODUCTION

Taylor-Couette (TC) flow between two differentially rotating coaxial cylinders is widely used as a basic model to study a variety of fluid dynamical problems, including instabilities, turbulence, and mixing. One of the most important processes in magnetized, differentially rotating fluids is the magnetorotational instability (MRI) which is a powerful dynamical instability arising from the interplay between a weak magnetic field and differential rotation with radially decreasing angular velocity $\partial_r \Omega < 0$. MRI was first theoretically found in an unbounded TC setup with an ideally conducting fluid by Velikhov [1] in 1959 and then rediscovered about three decades later, in 1991, by Balbus and Hawley [2] as a central mechanism responsible for angular momentum transport and mass accretion in astrophysical disks. In a TC setup, the flow profile can be configured by adjusting the rotation rates of the cylinders such that the angular velocity of the fluid Ω between the cylinders approximately

matches the Keplerian rotation profile, $\Omega \propto r^{-3/2}$, of the disks [3–5], where r is the radius. These astrophysically relevant profiles are characterized by radially decreasing angular velocity, $\partial_r \Omega < 0$, and increasing specific angular momentum, $\partial_r (r^2 \Omega) > 0$, referred to as a quasi-Keplerian regime, which is hydrodynamically stable according to Rayleigh’s centrifugal criterion [6, 7]. Furthermore, using a conducting fluid, such as liquid metals, in this quasi-Keplerian TC flow enables to study the interplay between magnetic fields and flow, in particular, magnetohydrodynamic (MHD) instabilities, such as MRI or current-driven Tayler instability, which are central in astrophysics [8]. Thus, TC setup represents a physically convenient model to investigate theoretically, numerically and experimentally (magneto)hydrodynamic instabilities of astrophysical importance.

A main challenge in the study of MRI in TC experiments has been to minimize the effects of endcaps covering the top and bottom ends of a finite-length TC device. These walls can have a significant impact on the flow structure and its overall dynamics (see the recent review by Ji and Goodman [6]), in the worst case inflicting the desired hydrodynamic stability. Due to the boundary conditions near the endcaps, the imbalance

* a.mishra@hzdr.de

among the pressure, Coriolis, and viscous forces leads to a poloidal motion of fluid, called secondary Ekman circulation (pumping), and the formation of associated boundary layers, called Ekman layers. Furthermore, the presence of one or more angular velocity jumps at the endcaps is virtually unavoidable, leading to localized regions of strong shear. The combination of Ekman circulation, redistributing angular momentum, and local shear can modify the primary angular velocity profile, and lead to the development of secondary hydrodynamic instabilities, unrelated to but interfering with MRI. There have been numerous attempts to mitigate these effects in TC experiments in order to ensure the stability of flow and maintain a consistent flow profile as close as possible to the classical, or ideal (i.e., with infinitely long cylinders) TC flow profile [9, 10]. Specifically, in the experiments, Ekman circulation is generally reduced by splitting the endcaps into two or more segmented sections. These sections are known as rims, if they are rotating solidly with the lateral walls, and rings when they rotate with their own angular velocity, which is usually between those of the inner and outer cylinders' rotation [6]. Such a differentially rotating segmented endcap design allows for the offset of differences between the fluid velocities in the vicinity of the endcaps, which rotate with the latter (due to the no-slip boundary condition), and the bulk flow, thereby reducing the penetration depth of Ekman circulation into the flow. In principle, dividing endcaps into as many independent segments as possible would be desirable in order to better approach the ideal TC flow profile and minimize Ekman circulation, which is, however, hard to realize in practice.

The main interest in these experiments with finite-height TC flows lies in sufficiently high magnetic Reynolds numbers, $Rm \gtrsim 10$, for exciting MRI [11–14]. The liquid metals used therein are characterized by very small magnetic Prandtl numbers, $Pm = \nu/\eta \sim 10^{-6} - 10^{-5}$, where ν is the kinematic viscosity and η magnetic diffusivity, and therefore the resulting Reynolds numbers Re should be as high as $Re \gtrsim 10^6$. Following the proposal of Ji et al. [15] for the MRI-experiment with gallium, several theoretical and numerical works addressed the flow dynamics in the finite-height TC setups, analyzing the effects of endcaps with different configurations. Kageyama et al. [9] studied both numerically and experimentally the hydrodynamic TC flow in a wide gap between the cylinders with small aspect ratio where the endcaps corotate with the outer cylinder up to $Re \sim 10^3$ in those for the simulations. They showed that in this configuration, the azimuthal flow profile was significantly modified from that of ideal TC profile and strong Ekman circulations were observed. Hollerbach and Fournier [16] studied the effect of both rigid endcaps attached to one of the cylinders and split endcaps with independently rotating rings on the flow structure and dynamics in a rapidly rotating and tall TC setup (height 5 times larger than the gap size) at $10^4 \leq Re \leq 10^6$. To reach these extreme parameters, they assume very

weak differential rotation, i.e., small Rossby numbers $Ro = (\Omega_{in} - \Omega_{out})/\Omega_{out} \approx 0$, where Ω_{in} and Ω_{out} are the angular velocities of the inner and outer cylinders, respectively. They showed that the endcaps play a crucial role in the overall structure of the established flow and that rigid endcaps would require very large aspect ratios (more than 100) in order to substantially mitigate the effects of Ekman circulations. Alternatively, the split-ring design of the endcaps can considerably reduce the Ekman circulation and a TC setup would probably require up to ten split rings for maintaining flow stability at high $Re \sim 10^6$. Their study highlighted the significance of Stewartson layers arising due to the discontinuity of the angular velocity at the split-rings, which at sufficiently high Ro can be prone to Kelvin-Helmholtz instability. The latter can interfere with MRI when a magnetic field is applied, complicating its dynamics. Therefore, it is important to first understand the TC flow dynamics (instabilities) in the hydrodynamic quasi-Keplerian case with finite differential rotation ($Ro \sim 1$) required for MRI, before moving to the MHD case.

Later, Burin et al. [17] demonstrated in the Princeton Hydrodynamic Turbulence Experiment (HTX) that splitting the top and bottom endcaps into three rings, where the inner rings rotate with the inner cylinder, the outer rings rotate with the outer cylinder, while the middle rings rotate independently, significantly reduces the Ekman circulation in the bulk of the flow. In the following experiments, the optimization of the angular velocity of the independent middle ring was performed [18–21], achieving a flow profile that approximate the ideal (i.e., axially unbounded) TC flow. Numerical simulations at Re much lower than experimental values, confirmed the reduction of Ekman circulations in the three-ring setup [4, 5, 22]. These simulations also showed that the considered quasi-Keplerian TC flow is overall hydrodynamically stable (except for some turbulence in the thin boundary layers) and hence does not lead to an efficient transport of angular momentum consistent with the earlier experiments [3].

Other TC setups with large aspect ratios and endcaps co-rotating with the outer cylinder were studied in multiple experiments in the quasi-Keplerian rotation regime [23–25]. However, contrary to the Princeton HTX experiment in both the Maryland [23, 24] and Twente [25] experiments, the measurements in the middle part of the flow indicated transport of angular momentum for the quasi-Keplerian flows. Simulations then showed that in these experiments large deviations in the flow profile from the ideal TC profile occurred at large Re due to strong Ekman circulations which apparently gave rise to the instability in the bulk flow and resulting angular momentum transport [5].

In this paper, we focus on the hydrodynamic evolution of the TC flow specifically for the upcoming DRES-DYN-MRI experiment with liquid sodium [26], which is currently under construction at the Helmholtz-Zentrum Dresden-Rossendorf (HZDR) aiming to detect

and study various types of MRI in the laboratory. To reduce the Ekman circulations in this experiment, the endcap is split into two outer and inner rims each firmly attached to the respective cylinder. Such a configuration of the endcaps was previously analyzed both theoretically and experimentally in the quasi-Keplerian regime. In the early experiments by Wendt [27], the endcap was split at a mid-point for which no transition to turbulence was reported [27, 28] for the values of Re ranging from 50 to 10^5 , although the torque obeyed a power-law scaling with Re . By contrast, Richard and Zahn [29] reanalyzed the data of Wendt [27] and reported turbulence, which was attributed to the finite amplitude instability at large $Re \sim 10^5$. Later, this split-ring endcap configuration was studied numerically for the PROMISE experiment by Szklarski [30], who demonstrated an efficient reduction in Ekman circulation if the endcaps are split at a distance $0.4r_{\text{in}}$ from the inner cylinder (with radius r_{in}) instead at the mid-point. Another focus of that paper was on the specific role of an axial magnetic field and the emerging Ekman layers. Since, fortunately, the results of this optimization did not depend much on the Hartmann number, this setup was indeed implemented in the PROMISE experiment, confirming the reduction in Ekman circulations in the bulk flow [10]. Yet, as the PROMISE experiment is limited to $Re \lesssim 10^4$ by construction, the effectiveness of this endcap configuration (with a ring slit at a radius $1.4r_{\text{in}}$) in reducing Ekman circulations could not be tested for higher $Re \sim 10^6$, needed for MRI in liquid metal TC flows. At such high Re , Ekman and Stewartson layers can become unstable and turbulent, complicating the flow dynamics and interfering with the MRI mode, which in turn makes it hard to unambiguously identify the latter in the experiments [31, 32].

The main goal of this study, intended as preparatory for the upcoming DRESHDYN-MRI experiment, is to understand the flow structure and dynamics in the DRESHDYN-TC device under the influence of endcaps for a wide range of Reynolds numbers up to $Re \sim 10^5$ for the quasi-Keplerian rotation (i.e., $\partial_r \Omega < 0$, $\partial_r(r^2 \Omega) > 0$) relevant for astrophysical disks first in the purely hydrodynamic regime, without magnetic fields. In particular, we will characterize the properties of Ekman and Stewartson layers as well as Ekman circulations, arising from these layers as the flow encounters cylinder walls, as a function of Re . This will in turn form the basis for the subsequent MHD study of the flow upon which MRI emerges when an axial magnetic field is present.

The paper is organized as follows. The basic equations, problem formulation and numerical setup are given in Sec. II. The main results on the flow structure, boundary layer scalings, effects of varying cylinder rotations and implications for MRI are presented in Sec. III. Conclusions are given in Sec. IV.

II. PHYSICAL MODEL

We consider a TC setup axially bounded by the top and bottom endcaps where the inner and outer cylinders have radii r_{in} and r_{out} , height L_z and rotate at angular velocities Ω_{in} and Ω_{out} , respectively [Fig. 1(a)]. In the case of an axially unbounded setup (infinitely long cylinders), this would give rise to the differential rotation of the fluid between the cylinders with the ideal TC angular velocity profile,

$$\Omega_{\text{TC}}(r) = \frac{\Omega_{\text{out}} r_{\text{out}}^2 - \Omega_{\text{in}} r_{\text{in}}^2}{r_{\text{out}}^2 - r_{\text{in}}^2} + \frac{(\Omega_{\text{in}} - \Omega_{\text{out}}) r_{\text{in}}^2 r_{\text{out}}^2}{r_{\text{out}}^2 - r_{\text{in}}^2} \frac{1}{r^2}. \quad (1)$$

The corresponding profile of the azimuthal velocity $u_{\phi}^{\text{TC}} = \Omega_{\text{TC}} r$ is depicted in Fig. 1(b). The DRESHDYN-TC device considered here has endcaps split at a radius $r_s = 1.4r_{\text{in}}$ [Fig. 1(c)], which was shown to result in the efficient mitigation of Ekman circulation for the scaled-down PROMISE device [30]. Investigations on whether split-position radius different from $1.4r_{\text{in}}$ might be even better suited are presently ongoing. The inner and outer rims rotate with the angular velocities of the inner and outer cylinders, respectively, as seen in Figs. 1(a) and 1(c). At the top and bottom boundaries, the azimuthal velocity (piecewise) linearly increase with radius on either side of a jump, which occurs at the split radius [Fig. 1(b)].

The incompressible flow of a Newtonian fluid is governed by the Navier-Stokes equations,

$$\frac{\partial \mathbf{u}}{\partial t} + (\mathbf{u} \cdot \nabla) \mathbf{u} = -\frac{1}{\rho} \nabla P + \nu \nabla^2 \mathbf{u}, \quad (2)$$

$$\nabla \cdot \mathbf{u} = 0, \quad (3)$$

where \mathbf{u} is the fluid velocity, P is the pressure, while the density ρ and kinematic viscosity ν of the fluid are both spatially constant. The velocity boundary conditions at the walls and the endcap rims are no-slip.

We non-dimensionalize time by Ω_{in}^{-1} , angular velocities by Ω_{in} , length by the gap width between the cylinders, $d = r_{\text{out}} - r_{\text{in}}$, and velocity by $\Omega_{\text{in}} d$. The main parameters of the problem are the Reynolds number $Re = \Omega_{\text{in}} d^2 / \nu$ and the ratio of the angular velocities of the cylinders $\mu = \Omega_{\text{out}} / \Omega_{\text{in}}$. The definition of Re corresponds to the inverse of the Ekman number, $Re = Ek^{-1}$, used for rapidly rotating flows. In the DRESHDYN-TC device, the ratio of the cylinder radii is fixed to $r_{\text{in}} / r_{\text{out}} = 0.5$ and the aspect ratio to $\Gamma = L_z / d = 10$. A full set of the parameters of the DRESHDYN-MRI experiment are presented in [13], while in this paper we consider the astrophysically important quasi-Keplerian rotation with $\partial_r \Omega < 0$ and $\partial_r(r^2 \Omega) > 0$ and hence stable according to Rayleigh's centrifugal criterion (for infinitely long cylinders), which using Eq. 1, implies $r_{\text{in}}^2 / r_{\text{out}}^2 < \mu < 1$.

We solve Eqs. (2) and (3) using the spectral element code SEMTEX [33, 34] in cylindrical coordinates (r, ϕ, z) , which is based on a continuous-Galerkin nodal spectral

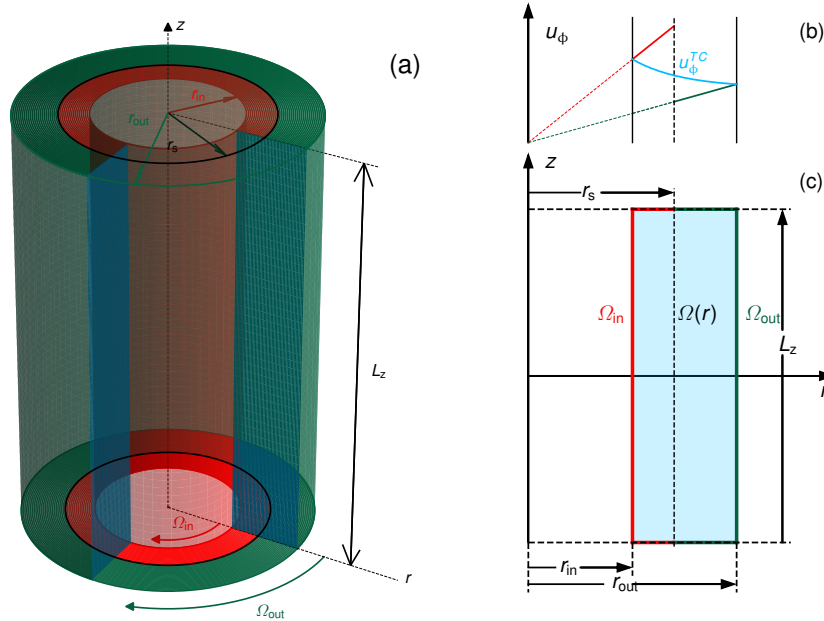


FIG. 1. (a) TC setup with the split endcaps and (c) its 2D section in the meridional (r, z) -plane. The outer wall and the corresponding rim are in dark green, while the inner wall and the corresponding rim are in red. (b) The radial profile of the rims' azimuthal velocities plotted together with the ideal unbounded TC profile in light blue.

TABLE I. List of all the simulations done and the corresponding values of Re , μ and the number of radial n_r and axial n_z elements. The parameter values used for resolution study are highlighted in grey.

$10^{-3}Re$	μ	n_r	n_z
1, 4, 7, 10, 20, 40, 75, 100	0.27	21	201
1, 4, 7, 10, 20, 40, 75, 100	0.30	21	201
1, 4, 7, 10, 20, 40, 75, 100, 200	0.35	21	201
20, 40, 75, 100, 200, 400, 600	0.35	31	201
100, 200, 400, 600	0.35	41	201
1, 10, 100, 200	0.40	21	201
1, 10, 100, 200	0.45	21	201
1, 10, 20, 40, 100, 200	0.50	21	201

element method (SEM) in the 2D meridional (r, z) -plane and Fourier expansion in the azimuthal ϕ -direction to provide 3D solutions [33, 34]. Table I lists all the simulations carried out in this study with the corresponding Reynolds numbers, ratio of cylinders' angular velocities μ and numerical resolutions (n_r, n_z) , indicating the number of elements in the radial and axial directions, respectively. The order of the polynomial basis functions in the spectral discretization is fixed to 9. Resolution tests and the comparison of the code results with a finite element code are discussed in Appendix A.

In this first hydrodynamic investigation for the DRESYDYN-MRI experiment, we consider only axisymmetric $(\partial_\phi = 0)$ perturbations. Limiting our study to

axisymmetric modes offers benefits for computing efficiency, thereby allowing for a more extensive parametric survey. This enables us to investigate the dynamics also at very high $Re \gtrsim 2 \times 10^5$. Moreover, in the context of the DRESYDYN-MRI experiment, the axisymmetric mode is of central interest, since it is the most unstable mode of MRI [13, 35, 36]. Consequently, the primary goal of this study is to understand the evolution of axisymmetric perturbations in a finite-length TC setup having the endcap configuration similar to that in DRESYDYN-TC device, which can be later generalized to non-axisymmetric perturbations. This approach leads to two distinct scenarios: Firstly, in cases where the axisymmetric flow exhibits instability (turbulence) due to endcaps, it is expected that the non-axisymmetric flow would similarly display instability given that perturbations resulting from the endcaps lack any modal preference. Secondly, in parameter regimes where axisymmetric flow is stable, our future efforts may concentrate on investigating the dynamics of non-axisymmetric modes. Assuming axisymmetry of the flow to examine the effects of the endcaps on flow dynamics in the Rayleigh-stable regime should establish an upper limit for the instability strength, as inclusion of non-axisymmetric modes would offer additional degrees of freedom for instability dissipation in the flow.

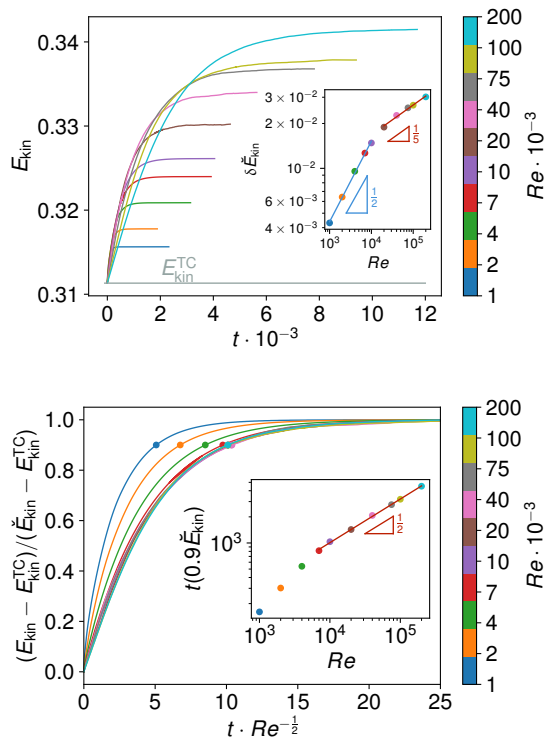


FIG. 2. (a) Evolution of the volume-averaged kinetic energy at different Re whose saturated values $\delta \dot{E}_{\text{kin}}$ scale with Re as shown in the inset. (b) Evolution of the rescaled kinetic energy with the inset showing the scaling of time to reach 90% of the quasi-steady saturated state.

III. RESULTS

We study the evolution of the TC flow in the Rayleigh-stable regime, taking the TC profile Ω_{TC} from Eq. (1) as an initial state, $\mathbf{u}(t=0) = \Omega_{\text{TC}} r e_\phi$. Since the latter is a stationary solution in the case of the axially unbounded cylinders, its subsequent evolution is due to the adjustment near the axial boundaries as a result of the no-slip boundary condition. Specifically, the velocity difference between the fluid attached to and hence rotating with the endcaps and the bulk azimuthal flow causes imbalance between pressure and centrifugal forces, which in turn induces radial velocity u_r in the vicinity of the axial boundaries. This imbalance results in the formation of Ekman layers, which, when turning near the cylinder walls, give rise to Ekman circulations penetrating deeper into the bulk flow [6, 17]. Throughout Sec. III.A-III.C we fix $\mu = 0.35$, whereas the dependence of the results on varying μ is analyzed in Sec. III.D.

A. Flow structure and evolution

Figure 2(a) shows the evolution of the volume-averaged kinetic energy $E_{\text{kin}} = (1/2V_f) \int u^2 dV$, where V_f is the

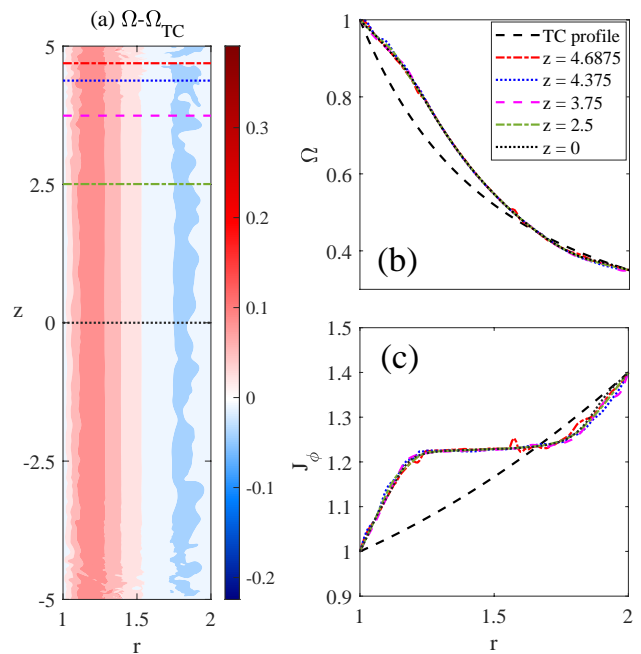


FIG. 3. (a) Deviation, $\Omega - \Omega_{\text{TC}}$, of the angular velocity Ω from the ideal one Ω_{TC} in the (r, z) -plane and (b) the radial profiles of Ω at different z [marked by horizontal lines in (a)] in the saturated state at $Re = 2 \times 10^5$. (c) The specific angular momentum $J_\phi = r u_\phi$ vs. r at the same height as in (b).

total volume of the flow domain between the cylinders. Initially it is independent of Re and determined by the ideal TC profile (Eq. 1), depending only on μ (at a given $r_{\text{in}}/r_{\text{out}} = 0.5$ used here). Due to the driving by the endcaps, the kinetic energy initially increases during the adjustment phase and eventually saturates to a nearly constant value \dot{E}_{kin} . The perturbed kinetic energy $\delta \dot{E}_{\text{kin}} = \dot{E}_{\text{kin}} - E_{\text{kin}}^{\text{TC}}$, where $E_{\text{kin}}^{\text{TC}} = E_{\text{kin}}(t=0)$ is the energy of the initial TC flow, increases with Re as a power law, as seen in Fig. 2(a). We identify two power-law behaviors for laminar and turbulent regimes with exponents $1/2$ and $1/5$, respectively. Also, the larger is Re , the longer is the saturation time [Fig. 2(b)]. For $Re > 10^4$, the time at which the system reaches 90% of the saturation value occurs at $10\sqrt{Re}$, consistent with the scaling of spin-up time at small Ekman numbers [37].

Thus, although the ideal TC flow profile valid for infinitely long cylinders is independent of Re , the overall structure of the saturated (established) flow under the influence of the endcaps and the corresponding value of \dot{E}_{kin} depends on Re due to viscous adjustment. However, as seen in Fig. 2(a), the relative difference between \dot{E}_{kin} and that of Ω_{TC} remains small $\lesssim 10\%$.

Figure 3 shows the structure of the angular velocity $\Omega = u_\phi/r$ in the meridional (r, z) -plane and its radial profiles at different axial positions in the saturated state. [38] At high $Re = 2 \times 10^5$ (see also the $Re = 10^4$ case in Fig. 14 of Appendix), the deviation of Ω from the ideal one Ω_{TC} , i.e., $\Omega - \Omega_{\text{TC}}$ can be divided into two main,

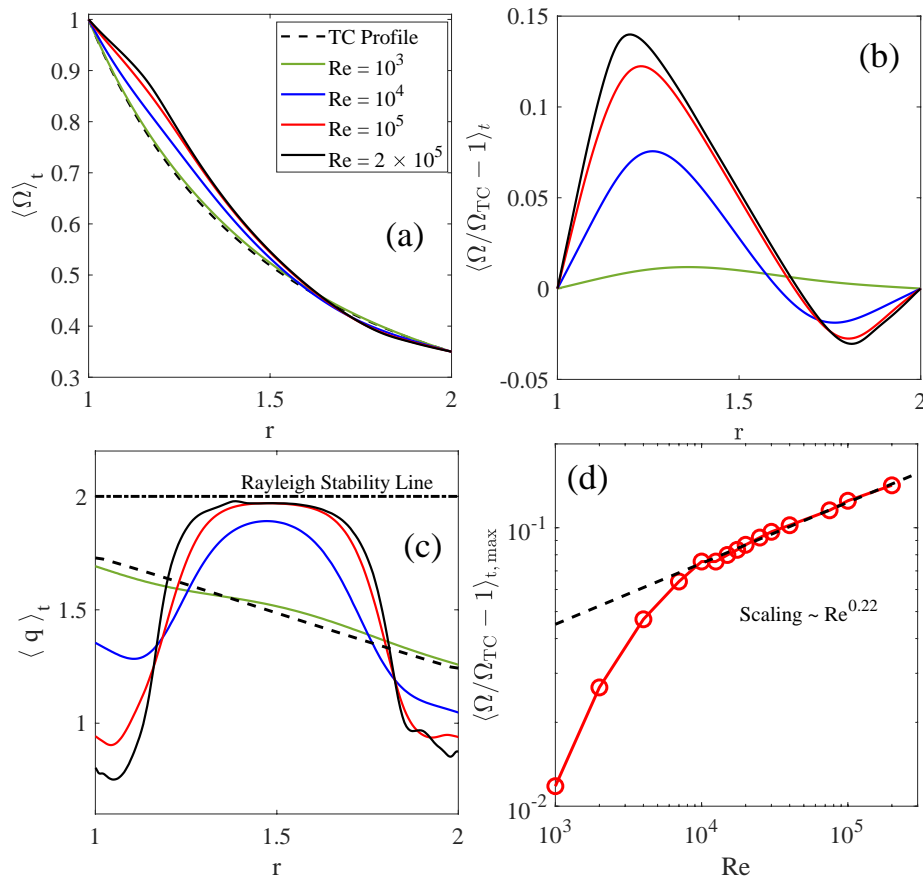


FIG. 4. Time-averaged profiles of (a) the angular velocity $\langle \Omega \rangle_t$, (b) its relative deviation, $(\langle \Omega \rangle_t / \Omega_{TC}) - 1$, from that of the ideal TC profile, Ω_{TC} , (c) the local shear parameter $\langle q \rangle_t = \langle -\partial \ln \Omega / \partial \ln r \rangle_t$ vs. r for $Re \in \{10^3, 10^4, 10^5, 2 \times 10^5\}$ at the mid-height $z = 0$. Black dashed and dot-dashed lines show q for the ideal TC flow and the Rayleigh-stability threshold $q_c = 2$, respectively, (d) Scaling of $(\langle \Omega \rangle_t / \Omega_{TC} - 1)_{t, \max}$ maximized over r at $z = 0$ as a function of Re . It follows the power-law $Re^{0.22}$ at high $Re \geq 10^4$, as indicated by the black dashed line.

positive (at $r \lesssim 1.5$) and negative (at $r \gtrsim 1.5$) parts. The first one being by absolute value larger than the second one, implying that the azimuthal flow is modified mostly in the inner part $r \lesssim 1.5$. At the split radius, the inner rim velocity displays the greatest deviation with respect to the TC profile, as shown in Fig. 1(b). On the other hand, this deviation is nearly uniform along z , i.e., axially independent, as is also seen from the almost identical radial profiles of $\Omega(r, z)$ at different z in Fig. 3(b). This is consistent with the Taylor-Proudman theorem, which states that rapidly rotating flows tend to align along the axis of rotation. By contrast, at small $Re = 10^3$, the perturbations with respect to Ω_{TC} are concentrated mostly near the endcaps while the bulk of the flow is essentially unchanged (see also Fig. 13 in Appendix).

To see the impact of changing angular velocity on the angular momentum transport, we show in Fig. 3(c) the radial profiles of the specific angular momentum $J_z = ru_\phi$ at different axial positions marked by the same colors as in Figs. 3(a) and 3(b). It shows that specific angular momentum is significantly increased (decreased) at those radii where the angular velocity Ω is larger (smaller) than

Ω_{TC} . The inner rim injects angular momentum, while the outer rim extracts it. Still, it can be seen that the angular momentum transport throughout the bulk of the flow is largely independent of the height, except very close to the endcaps, where boundary layers are present.

Due to the z -invariance, we can concentrate on the radial profiles at the mid-height ($z = 0$). As expected, the deviation from the unbounded ideal profile increases with the Reynolds number. This is visible in the time-averaged radial profiles of the angular velocity $\langle \Omega \rangle_t$, as depicted in Fig. 4(a) for $Re \in \{10^3, 10^4, 10^5, 2 \times 10^5\}$, with the black dashed line being the ideal TC profile Ω_{TC} . For $Re = 10^3$, the flow profile at the mid-height of the cylinder is very similar to the ideal profile Ω_{TC} . For higher $Re \geq 10^4$, the angular velocity is larger than Ω_{TC} , at $r \lesssim 1.5$, while for $r \gtrsim 1.5$ it remains smaller but close to the latter. To further quantify this deviation of the angular velocity, in Fig. 4(b) we show the time-averaged relative difference $\langle \Omega / \Omega_{TC} - 1 \rangle_t$, which increases with Re , becoming more positive. It reaches up to $\approx 14\%$ for $Re = 2 \times 10^5$ and, as noted above, is mainly located in the inner half of the gap width between the cylinders.

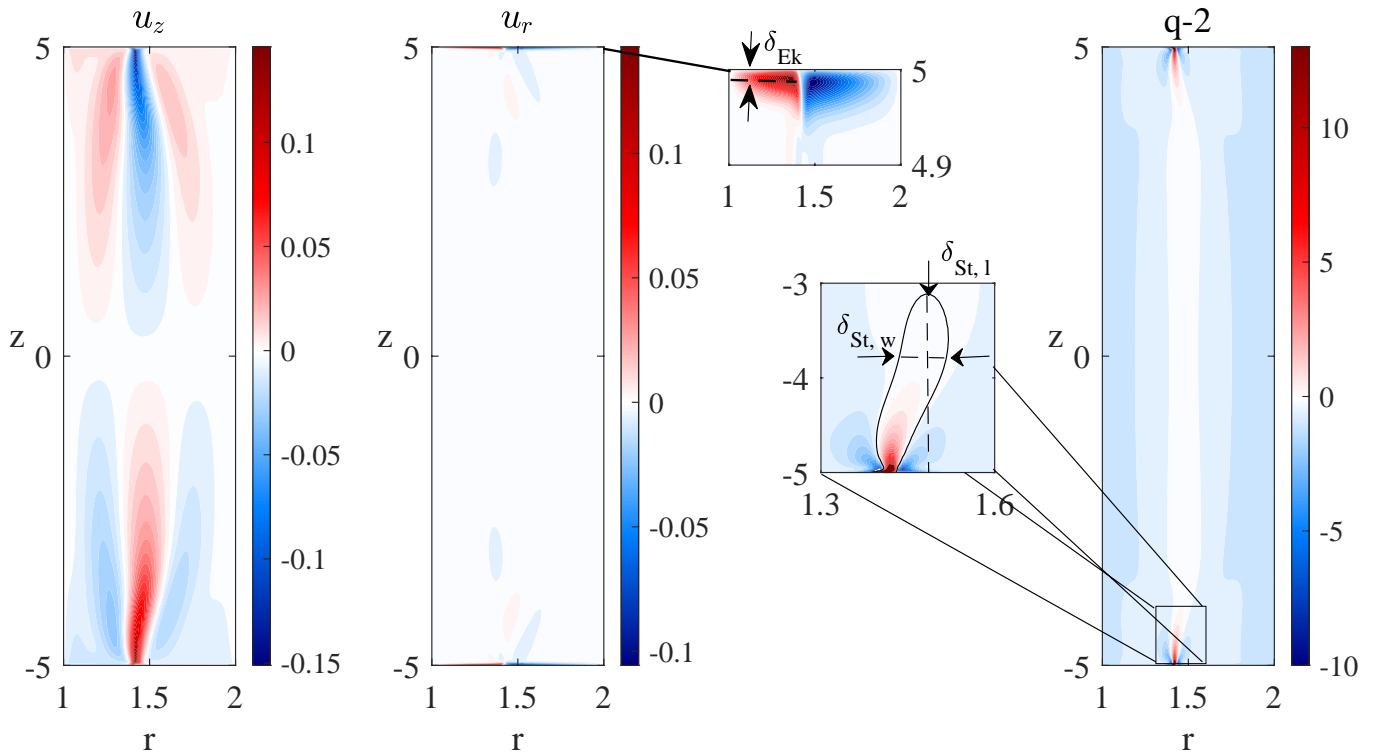


FIG. 5. Snapshots of the axial u_z (left) and radial u_r (middle) velocities in the meridional (r, z) -plane for $Re = 10^4$ in the saturated state. Top and bottom boundaries are symmetrical for this Re . Stable Ekman layers (with thickness δ_{Ek}) at the endcaps are better seen in the zoomed inset of u_r . Right panel shows the snapshot of the local shear parameter $q - q_c$ in the (r, z) -plane, where $q_c = 2$ is the critical value of Rayleigh-stability. Zoomed insets in this panel illustrate the vertical Stewartson layers (with width $\delta_{St,w}$ and length $\delta_{St,l}$) characterized by high shear $q \geq q_c$ (red area) near the endcaps.

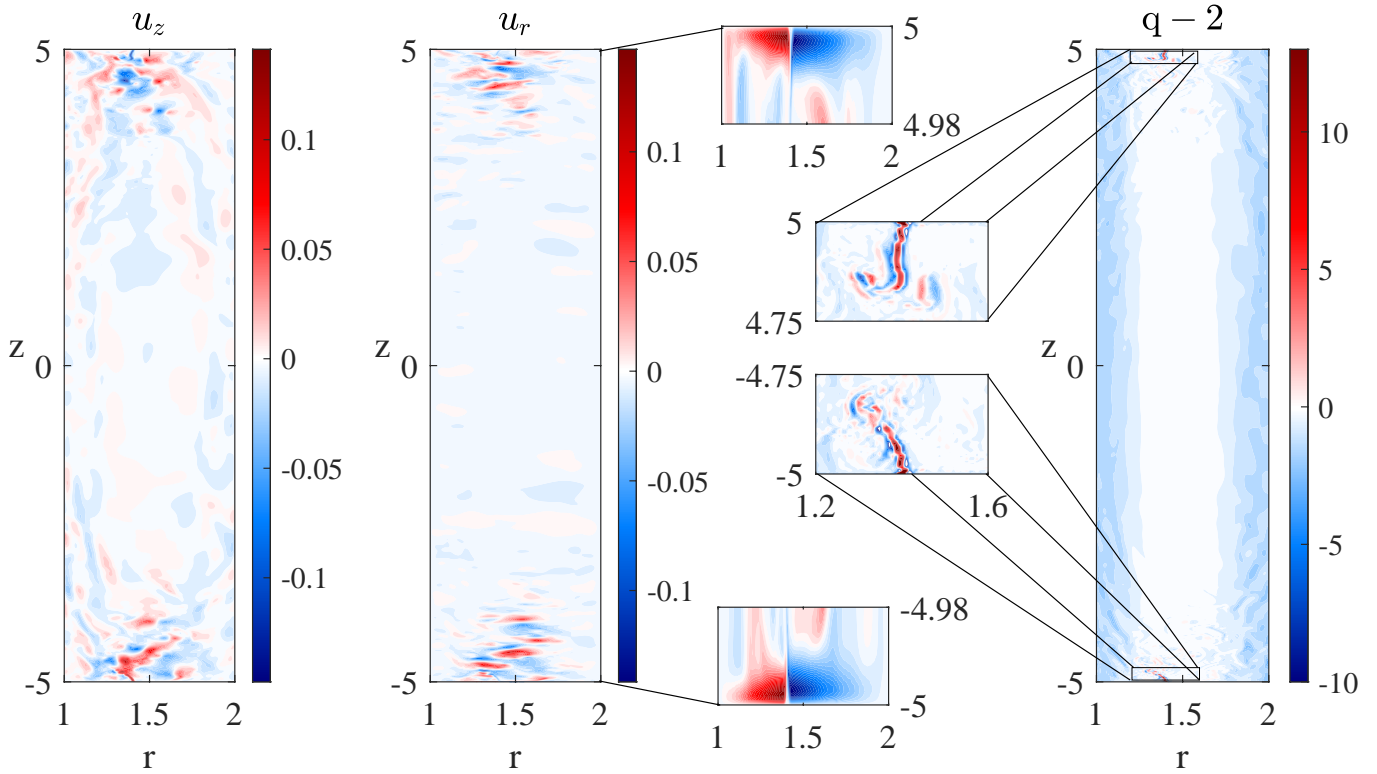


FIG. 6. Same as in Fig. 5 but for a more turbulent regime at $Re = 2 \times 10^5$.

To investigate the effect of angular velocity deviation on the stability of the flow, in Fig. 4(c) we show the radial profile of the time-averaged local shear parameter $\langle q \rangle_t = -\langle \partial \ln \Omega / \partial \ln r \rangle_t$ at the mid-height $z = 0$, which is also known as q -parameter in the TC literature [25]. This parameter plays an important twofold role: it determines the local centrifugal stability of the flow according to Rayleigh's criterion and, in the MHD regime, sets the growth rate and strength of MRI. The black dot-dashed line represents the marginal Rayleigh stability threshold $q_c = 2$ (i.e., $\partial_r(r^2\Omega) = 0$), such that at $q \leq q_c$ the flow is hydrodynamically stable. This condition is satisfied for all profiles at the mid-height of the domain, as seen in Fig. 4(c). For small $Re = 10^3$ the shear parameter almost linearly decreases with the radius and the flow profile is still quite similar to the TC profile. However, for higher $Re \geq 10^4$, the profile of $\langle q \rangle_t$ considerably changes to a hump shape, with a plateau around the mid radius, quite close to the critical q_c . Therefore, the bulk flow remains in the Rayleigh-stable regime, but nearly reaches the threshold of the marginal stability around $r \approx 1.5$.

This trend with Reynolds number holds across all the simulations. Figure 4(d) shows the maximum value of the relative deviation $(\langle \Omega \rangle_t / \Omega_{\text{TC}} - 1)_{\text{max}}$, which increases with increasing Re , first steeply at $Re \lesssim 10^4$ and then follows a power-law $Re^{0.22}$ at $Re \geq 10^4$. This scaling allows an extrapolation to even higher $Re \sim 10^6$ relevant to the DRESHDYN-MRI experiment, which as a result gives $(\langle \Omega \rangle_t / \Omega_{\text{TC}} - 1)_{\text{max}} \approx 16\%$. This behavior of q and perturbed angular velocity with Re depicted in Fig. 4 is useful for its direct applicability to the flow dynamics in the upcoming DRESHDYN-MRI experiment.

The split endcaps not only affect the azimuthal velocity but also generate radial and vertical motions, as seen in the meridional snapshot for $Re = 10^4$ in Fig. 5. The axial velocity u_z is highest close to the slit radius r_s and extend with typical patterns of coherent Ekman circulations into the bulk flow. By contrast, the radial velocity u_r is predominantly localized close to the endcaps, forming thin stable Ekman boundary layers there (see zoomed-in area in the plot of u_r), and is relatively weak in the bulk flow. Both u_r and u_z are much smaller than the total azimuthal velocity u_ϕ , but are comparable to its perturbation with respect to the initial TC profile, $u_\phi - u_\phi^{\text{TC}}$. Note the symmetric and antisymmetric characteristics of the radial and vertical velocities around $z = 0$, respectively. Such a degree of symmetry indicates that the perturbed flow at this Reynolds number still remains laminar.

To understand the flow stability, Fig. 5 also shows the distribution of the relative shear $q - q_c$ with respect to the marginal stability value $q_c = 2$ in the (r, z) -plane in the saturated state, indicating the locally stable ($q \leq q_c$, blue) and unstable ($q > q_c$, red) regions. In particular, the Ekman layers are stable, while the vertical shear, or Stewartson layers [16, 39] originating from the top and bottom endcaps at r_s are characterized by high shear q (red areas) and hence would be Rayleigh-unstable. How-

ever, viscosity appears to be sufficient to prevent disruption of these layers and allow them to extend deeper into the flow. We will see below that the situation dramatically changes at higher $Re \gtrsim 10^5$, when Ekman and Stewartson layers become unstable and turbulent.

Figure 6 shows the structure of u_r , u_z and q in the (r, z) -plane in the saturated state for $Re = 2 \times 10^5$. In contrast to the lower $Re = 10^4$ case above, now both velocity components exhibit irregular (turbulent) structures near the endcaps, which penetrate somewhat deeper into the flow. The zoomed version of u_r in the narrow vicinity of the endcaps shows that Ekman layers are much thinner but still laminar. Therefore, turbulence exhibited by poloidal velocity (u_r, u_z), starting near the endcap and penetrating deeper into the flow, results from the instability of the Stewartson layers emanating from the endcap-slits at r_s . Indeed, as seen from the corresponding distribution of $q - q_c$ in the (r, z) -plane on the rightmost panel of Fig. 6, these high shear $q > q_c$ layers (red) are distorted by the instability, not being hindered by viscosity. The instability, however, remains mainly localized near the endcaps at r_s .

So far we have characterized the structures of the azimuthal velocity, its shear q and the overall meridional flow. Let us now examine in a more quantitative manner the radial and axial profiles of the instantaneous radial and axial velocities at different Re , which are shown in Fig. 7. Initially, these velocities are zero and are produced during the adjustment phase by the endcap effects, extending farther from the latter into the bulk flow, down to the mid-height, in the form of Ekman circulations. As expected, both u_r and u_z increase by absolute value with increasing Re , but exhibit different behavior along r and z . It is seen in Figs. 7(a) and 7(b) that their variation with r becomes more irregular and stronger for higher Re , forming boundary layers with steep radial gradients (shear) near the inner and outer cylinder walls. This is associated with the presence of turbulence at $Re \gtrsim 10^5$, as already seen in Fig. 6, which is most intensive near the endcaps but also extends down to the mid-height.

Figure 7(c) shows the axial profile of the radially averaged poloidal velocity squared, $\int_{r_{\text{in}}}^{r_{\text{out}}} (u_r^2 + u_z^2) r dr$, for different Re in the saturated state. Note that for all the considered Re , strong shear is observed near the top and bottom endcaps (see zoomed-in insets) corresponding to thin Ekman layers discussed above, which increases with increasing Re . For smaller $Re \leq 10^4$, when turbulence is still absent, the poloidal circulation penetrates into the flow, with appreciable amplitude up to a quarter of the axial length from each side that monotonically decreases to a minimum value at $z = 0$. By contrast, as Re is increased further, turbulence sets in near the endcaps, as discussed above, and as a result the axial distribution of the poloidal circulation changes qualitatively. It becomes strongly concentrated and oscillatory near the endcaps but rapidly decays to very small values off the endcaps and remain almost independent of z at mid heights. This indicates that although Ekman circulations impact the

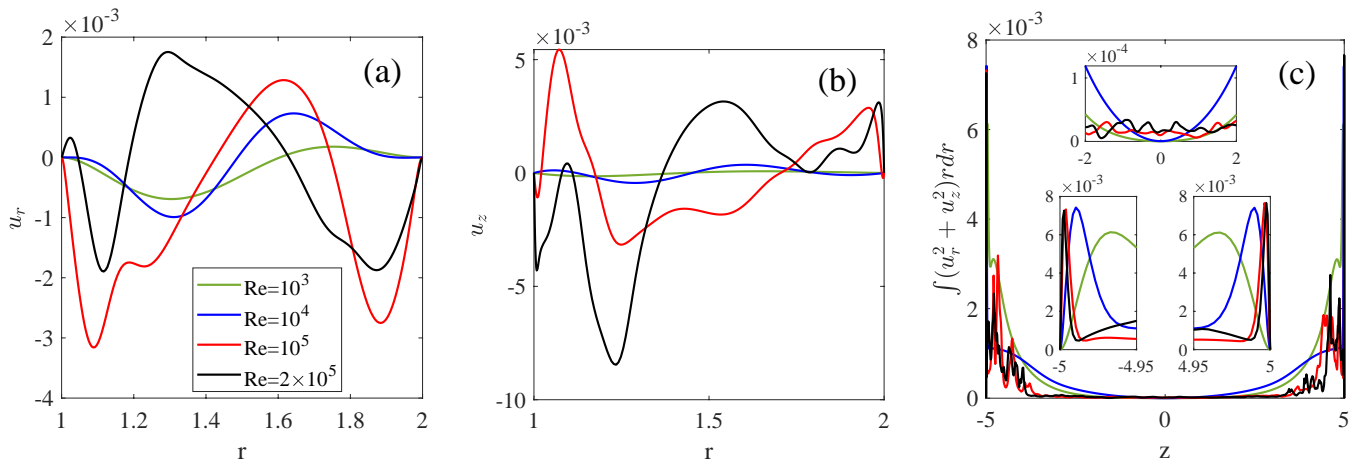


FIG. 7. Radial profiles of (a) the radial velocity u_r and (b) axial velocity u_z at the cylinder mid-height $z = 0$ in the saturated state for different Re . (c) Radially integrated squared poloidal velocity $\int(u_r^2 + u_z^2)rdr$ as a function of z for the same Re .

overall flow, their influence becomes more localized as Re increases, leaving a larger portion in the mid-height of the domain mostly unaffected.

B. Boundary Layer Scaling

In all studies of TC flows with axial boundaries, the Ekman boundary layer and its stability play a central role in the dynamics of the whole flow. The well-known scaling of a stable Ekman boundary layer thickness with Re given as $Re^{-0.5}$, which is a consequence of balance between the viscous and Coriolis forces, is widely discussed in the literature [16, 40, 41]. In the present setup, the endcaps divided into two rims rotating respectively with the angular velocities of the inner and outer cylinders give rise to two distinct Ekman layers near each ring (see insets in u_r plots of Figs. 5 and 6). We define the Ekman layer thickness as an axial distance from the endcap to the location of the maximum of the time-averaged u_r (see Fig. 5). Figure 8(a) depicts the Ekman layer thickness, δ_{Ek} , as a function of Re , which obey a power-law dependence $\delta_{Ek} \sim Re^{-0.52}$ and $\delta_{Ek} \sim Re^{-0.48}$ near the inner and outer rims, respectively. These scalings agree with the characteristic length of the laminar Ekman boundary layer, which implies that in the present setup these boundary layers remain stable, even for very high Re . The consistence of the scaling at higher Reynolds numbers can be due to the adoption of the time-averaged flow. Note also in this figure that due to the difference in the angular velocities of the endcap rims, the thickness of the boundary layer near the inner rim is smaller than that of the boundary layer near the outer rim, corresponding to the higher effective Re at the inner rim than at the outer one.

Let us now characterize the properties of the Stewartson layers emanating both from the top and bottom endcaps at the slit radius r_s due to the jump between

the angular velocities of the inner and outer rims. The layers have a maximum radial extent, or width $\delta_{St,w}$ and axial length $\delta_{St,l}$, as indicated in the rightmost panel of Fig. 5. In the stable (laminar) regime at $Re \leq 4 \times 10^4$, the shear layer is stationary with its width exhibiting a power-law dependence $\delta_{St,w} Re^{-1/4}$, as shown in 8(b), while in the turbulent regime at higher Re the scaling becomes $\delta_{St,w} \sim Re^{-0.15}$. At large Re , the dynamics and stability of Stewartson layer is important as it serves as the transition region between the azimuthal velocity near the endcaps and bulk of the flow. Spatial and temporal fluctuations within the Stewartson layer contribute to the deviation of its scaling from that in the laminar case. At any rate, one could expect that the transition of the Stewartson layer from a stationary (stable) to highly dynamic (turbulent) state implies also a change in its scaling properties.

Another feature of Stewartson layer is its ability to penetrate deeper into the bulk flow, as seen in the axial velocity map in Figs. 5 and 6. Previous investigations [42] conducted in different geometry have demonstrated that the length $\delta_{St,l}$ to which these layers extend into the flow increases linearly with Re . Figure 8(c) shows the dependence of this length as a function of Re in the present TC setup. For smaller $Re \leq 10^4$ this length increases with Re as a power-law $\delta_{St,l} \sim Re^{0.45}$. By contrast, for larger $Re \geq 10^4$, an interesting trend emerges where $\delta_{St,l}$ decreases with increasing Re , following a power-law $\delta_{St,l} \sim Re^{-0.6}$. This decreasing scaling with Re can be attributed to the instability of the Stewartson layers, which disrupting the latter into turbulence, reduces its length (Fig. 6). We will discuss this in more detail in the next section (see also Fig. 9).

In Figs. 8(a) and 8(c), we have also included the results of simulations at even higher $Re = 4 \times 10^5$ and $Re = 6 \times 10^5$, which although being close to a quasi-steady state, have not yet fully reached it (see Fig. 2). Therefore, these results are likely to undergo some modifications before

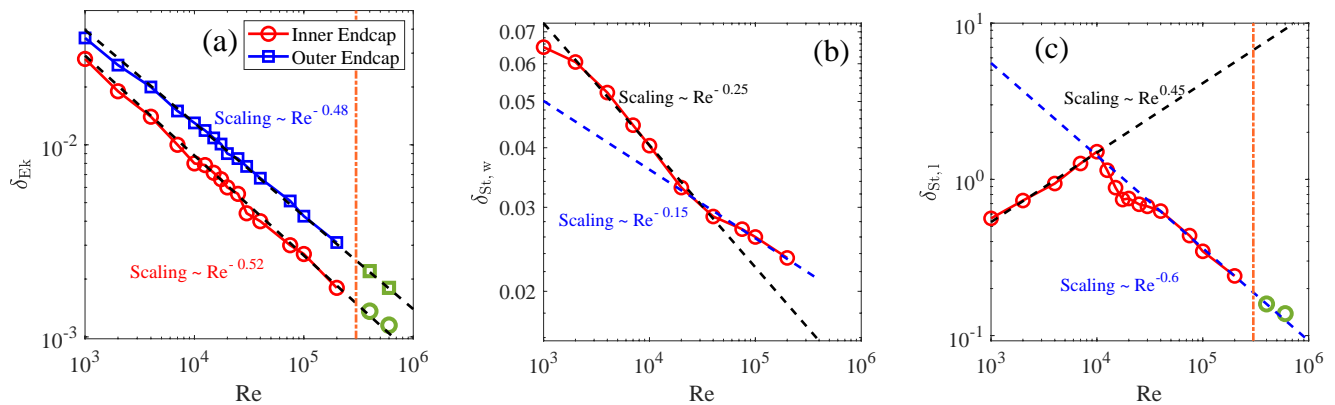


FIG. 8. (a) Ekman boundary layer thickness δ_{Ek} near the inner (red) and outer (blue) endcap rims as well as (b) the width $\delta_{St,w}$ and (c) length $\delta_{St,l}$ of the Stewartson layer as a function of Re . Dashed lines show the power-law fits. Vertical orange dot-dashed lines in (a) and (c) mark the maximum Re beyond which the simulations at $Re = 4 \times 10^5$ and $Re = 6 \times 10^5$ (green points) have not yet fully reached a quasi-steady state, but are close to the latter.

the flow reaches a final quasi-steady state (for this reason, we have not included them here). The boundary layers form during earlier stages of flow evolution and those near the endcaps are mainly responsible for driving the flow towards the quasi-steady state. The consistency of the data points at these Re with the scaling laws for the quasi-steady state at lower $Re \leq 2 \times 10^5$ in Figs. 8(a) and 8(c) strengthens this argument.

Finally, we note that these results on the stability of Ekman layers and unstable (turbulent) Stewartson layers at high Re , both remaining concentrated near the endcaps and rapidly decreasing in the bulk domain (see Fig. 7c), can be important for the upcoming DRESDYN-MRI experiment. In particular, the localization of perturbations near the endcaps and their relatively low level in the bulk flow can facilitate studies and identification of MRI modes.

C. Vortices

The flow becomes nearly stationary at smaller Re once the flow settles down in a saturated state (Fig. 5). By contrast, at higher Re , the flow is very turbulent (Fig. 6), involving the formation and evolution of vortices in the vicinity of the endcaps. Figure 9 shows azimuthal vorticity $\omega_\phi = (\nabla \times u)_\phi$ and the shear $q - q_c$ for $Re = 2 \times 10^5$ at different times in the saturated state. The vortices primarily emerge at the inner rim, near the slit radius r_s , due to the interplay of the Ekman and unstable, high-shear Stewartson layers. At time $t = 11563$, a typical large vortex (red spot near $(r, z) = (1.3, 4.8)$) surrounded by smaller scale vortices can be observed [Fig. 9(a)] corresponding to the site of the dynamic (“flapping”) Stewartson layer [Fig. 9(b)]. We can see that the structure of the Stewartson layer, including its length $\delta_{St,l}$, is determined (constrained) by the emergence of vortices of different scales, near the tail of the layer. Specifically, as the flow evolves, at $t = 11575$, the vortex near

$(r, z) = (1.3, 4.8)$ gets distorted [Fig. 9(c)] and so does the tail of Stewartson layer [Fig. 9(d)]. This deformed vortex then breaks up into a number of smaller-scale vortices, which propagate away from the endcaps into the bulk flow and gradually decay [Figs. 9(e) and 9(g)]. These smaller-scale vortices shed from the Stewartson layers in turn result in the disruption (cut-off) of these layers from a certain axial distance from the endcaps [Figs. 9(f) and 9(h)]. As a result, the scaling of their length is significantly altered from $\delta_{St,l} \sim Re^{0.45}$ in the laminar regime to $\delta_{St,l} \sim Re^{-0.6}$ in the turbulent regime, as seen in Fig. 8(c). After the small vortices migrate to the mid-height, this cycle of vortex formation, evolution and breakup starts again [Figs. 9(i) and 9(j)].

D. Effect of varying the angular velocity ratio μ

So far, the emphasis has been on studying the effect of endcaps at various Re for the quasi-Keplerian rotation of the cylinders with given $\mu = 0.35$. The above analysis clearly shows that at high enough $Re \gtrsim 10^4$ the shear layers induce turbulence, which is most intense near the endcaps and decreases into the bulk flow. The shear q at mid-height for such large Re always stays below, but close to, the marginal Rayleigh-stability threshold $q_c = 2$ [Fig. 4(c)]. Since the larger values of the rotation ratio μ can be reached in the DRESDYN-MRI experiment, here we explore how the above results change with μ .

For the ideal TC setup without endcaps, the flow becomes more and more stable as μ increases away from the Rayleigh-stability threshold (which is $\mu_c = 0.25$ in the present setup with $r_{in}/r_{out} = 0.5$). Figure 10(a) shows the radial profile of the time-averaged shear parameter $\langle q \rangle_t$ at the mid-height in the saturated state at different μ and the largest $Re = 2 \times 10^5$. Indeed, it is seen that the flow becomes overall more stable with q decreasing (at a given radius) as μ is increased. However, q at the slit radius r_s always remains close to, although slightly

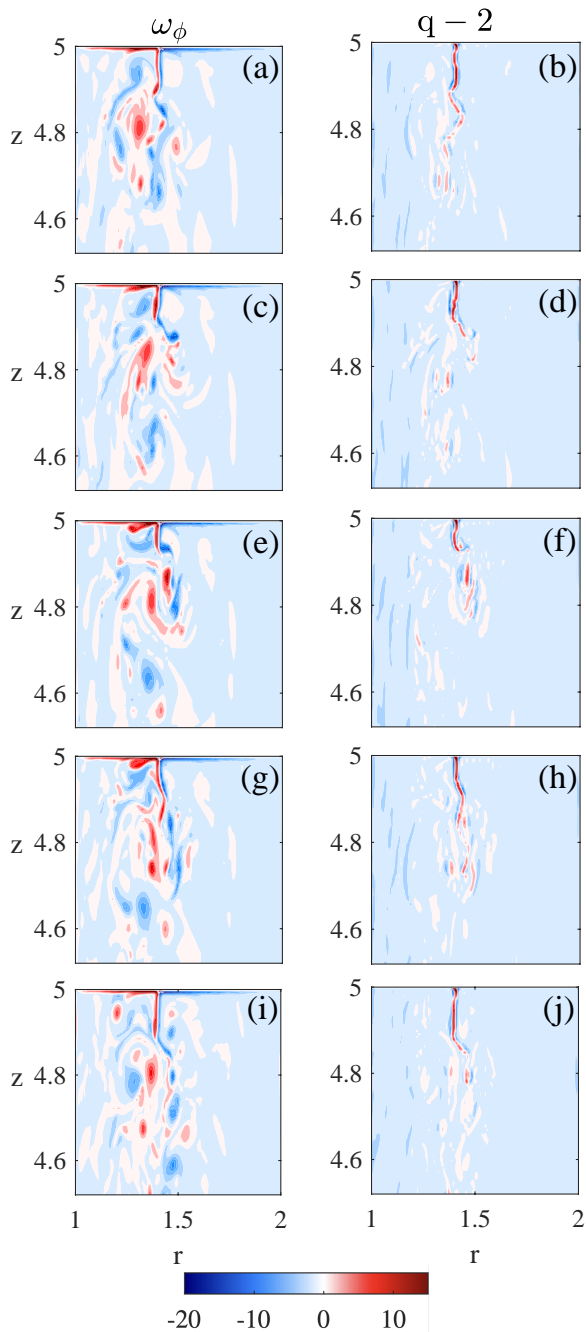


FIG. 9. Azimuthal component of vorticity $\omega_\phi = (\nabla \times u)_\phi$ (left column) and deviation, $q - q_c$ (right column), of the local shear q from the marginal stability threshold $q_c = 2$ in the saturated state for $Re = 2 \times 10^5$ at different times increasing from top to bottom: (a,b) at $t = 11563$, (c,d) at $t = 11575$, (e,f) at $t = 11578$, (g,h) at $t = 11580$ and (i,j) at $t = 11582$.

lower than, the Rayleigh-stability threshold due to the endcap effect regardless of the increase in μ .

The volume-averaged kinetic energy of the total flow in the quasi-steady state, \bar{E}_{kin} , as a function of μ at different Re is depicted in the top panel of Fig. 10(b). It increases linearly with μ for all the considered Re , which can be

attributed to the mean azimuthal flow. It is also evident from the bottom inset of Fig. 10(b) that the maximum of the kinetic energy of the perturbation, $\delta \bar{E}_{\text{kin}}$, is reached for μ between 0.3 and 0.35, while for larger μ the flow tends to be more stable. This is further supported by the following analysis of the Ekman and Stewartson layer properties with respect to μ .

Figure 10(c) shows the scaling of the Ekman layer thickness, δ_{Ek} , with μ for different Re at the outer endcap rim. [43]. It is seen that for smaller $Re \lesssim 10^4$, δ_{Ek} decreases with μ as a power-law $\mu^{-0.4}$, whereas for larger $Re \gtrsim 10^5$, this decrease becomes a little steeper $\mu^{-0.6}$. These exponents, which are close to $-1/2$, can be explained by simply considering the scaling of the Ekman boundary layer using Re computed with Ω_{out} , which still somewhat differ from each other in the laminar and turbulent regimes. Similarly, it is seen in Fig. 10(d) that the penetration length, $\delta_{St,l}$, of the Stewartson layers in the bulk flow decreases with increasing μ but differently in the laminar and turbulent regimes: in the first case at $Re \lesssim 10^4$, it follows the scaling $\delta_{St,l} \sim \mu^{-3.2}$, whereas in the second case at $Re \gtrsim 10^5$ the scaling is shallower $\delta_{St,l} \sim \mu^{-1}$, implying more stability at higher μ at this Re . Since in the envisioned DRESDYN-MRI experiment, the stability of the base flow before switching on a magnetic field is of great importance in order to unambiguously identify MRI modes, increasing μ to larger values (say, $\mu = 0.5$, but still not too large to suppress MRI) in this experiment, might be a viable possibility to ensure hydrodynamic stability of the flow.

E. Implications for MRI

As shown above, the structure and dynamics of a finite-height TC flow at large Re can be strongly affected by the Ekman circulations and unstable shear layers. In particular, we have also shown that higher μ increase hydrodynamic stability of the flow which can be favorable for the identification of MRI. On the other hand, larger μ is challenging as it significantly increases the critical values of Lundquist $Lu = B_{0z}d/\eta\sqrt{\rho\mu_0}$ and magnetic Reynolds $Rm = \Omega_{\text{in}}d^2/\eta$ numbers for the onset of MRI in experiments [13], where B_{0z} is the applied constant axial magnetic field, η magnetic diffusivity and μ_0 magnetic permeability of vacuum. Since in the upcoming DRESDYN-MRI experiments the technically reachable maximum values of these two numbers are $Lu_{\text{max}} = 10$ and $Rm_{\text{max}} = 40$, it is worthwhile to examine whether MRI can be achieved in these experiments despite higher μ for the radial profile of the angular velocity modified from the ideal TC one by the endcap effects.

For this purpose, following our previous studies [13, 44, 45] and a related recent study for the Princeton MRI-experiment [46], we carry out linear stability analysis of the corresponding MHD problem for equilibrium states with an imposed axial field B_{0z} and two different radial profiles of the angular velocity – an ideal TC profile

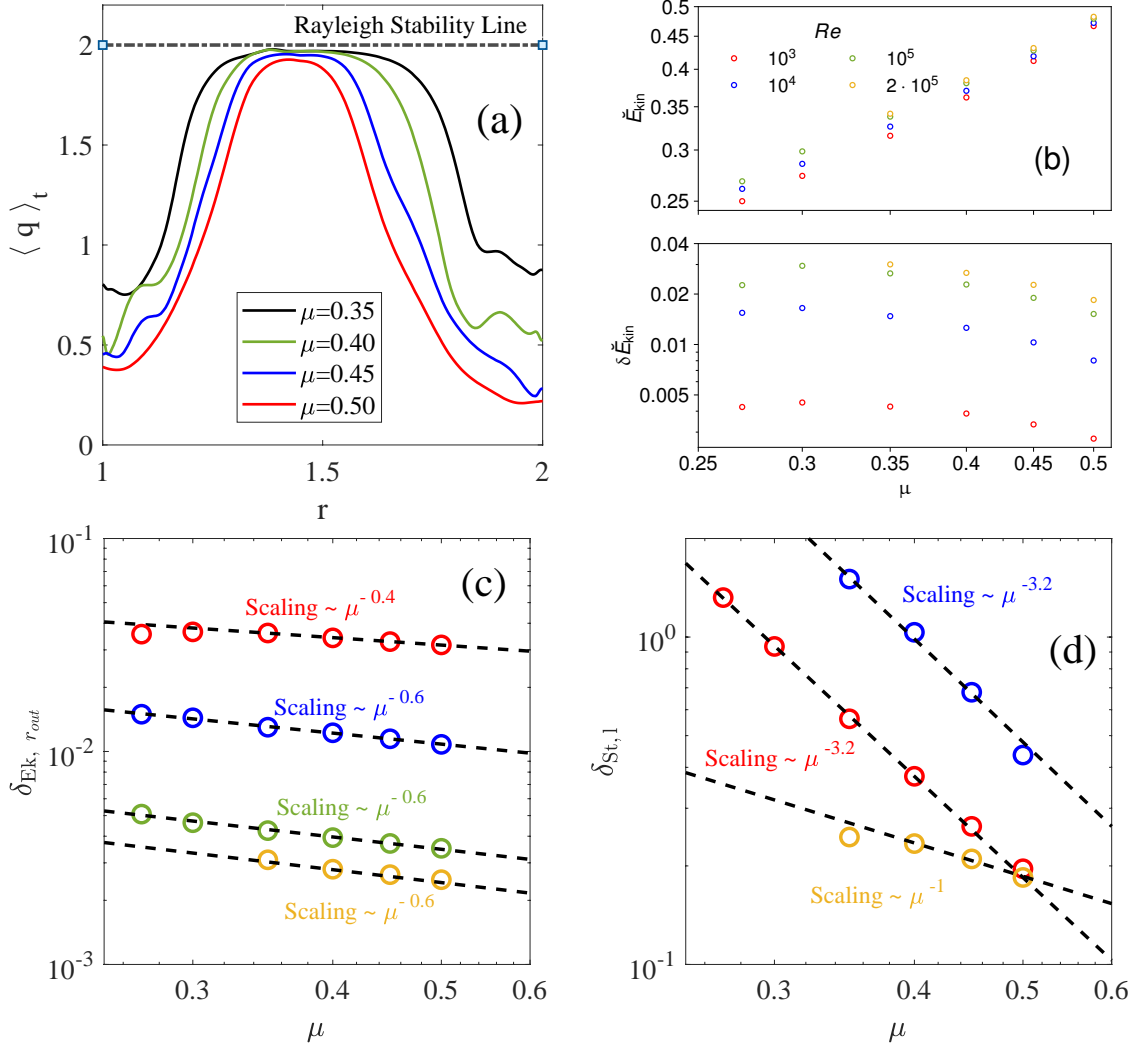


FIG. 10. (a) Radial profile of the time-averaged shear parameter $\langle q \rangle_t$ in the saturated state at the mid-height $z = 0$ for $Re = 2 \times 10^5$ and different μ . Scaling behavior of (b) the volume-averaged kinetic energy of the total flow \check{E}_{kin} and the perturbations $\delta \check{E}_{kin}$, (c) Ekman layer thickness, $\delta_{Ek, r_{out}}$, near the outer endcap rim and (d) Stewartson layer length, $\delta_{St,1}$, vs. μ for different Re in the saturated state. The black dashed lines in (b), (c) and (d) show the power-law fits.

Ω_{TC} and actual profile Ω at mid-height in the presence of endcaps from the above simulations at $Re = 2 \times 10^5$ and $\mu \in \{0.35, 0.5\}$ [Fig. 11(a)], which is more relevant to a real experimental situation. We then compare the onset criterion of MRI obtained for these two equilibria. Assuming axisymmetric perturbations of the modal form $\propto \exp(\gamma t + k_z z)$, we solve linearized MHD equations together with no-slip for velocity and insulating for magnetic field boundary conditions at the cylinder walls to find the growth rate γ . [47] For simplicity, periodic boundary conditions are adopted in the axial z -direction based on the fact that at large Re the angular velocity is nearly uniform in z (Fig. 3).

The resulting marginal stability (i.e., $\gamma = 0$) curves for the onset of MRI in the (Lu, Rm) -plane obtained for the ideal and modified TC profiles, are shown in Fig. 11(b).

These curves give the critical Lu and Rm for the onset of MRI, which appear to decrease with decreasing μ (see also [13]). The main result is that the modified profile of the angular velocity results in the considerably lower critical values of Lu and Rm than those for the ideal TC profile Ω_{TC} (see Table II). While this is favorable for the upcoming DRESHDYN-MRI experiments, since MRI may set in at lower Lu and Rm , which can be achieved with less efforts and energy expenses, it may also query the direct comparability of the experimental results with the original problem of MRI in Keplerian flows.

Wang et al. [46, 48, 49] reported MRI in the Princeton TC setup at much (about 3 times) lower Lu and Rm than dictated by 1D linear stability analysis in an ideal TC flow. This was attributed to the modification of the mean Ω profile by the electrically conducting end-

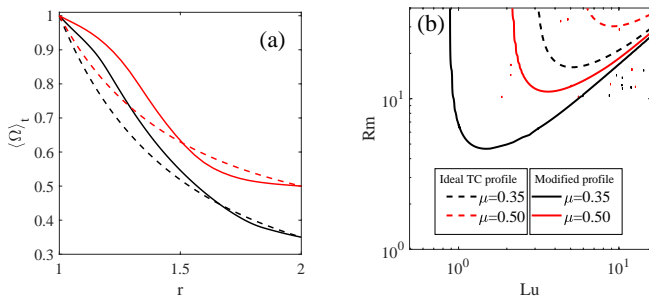


FIG. 11. (a) Radial profile of the time-averaged angular velocity $\langle \Omega \rangle_t$ in the saturated state at $z = 0$ for $\mu = 0.35$ (black) and 0.5 (red) for infinitely long cylinders given by Eq. 1 (dashed) and in the presence of endcaps (solid) at $Re = 2 \times 10^5$. (b) Marginal stability curves of MRI in the (Lu, Rm) -plane (the area above these curves is MRI-unstable) obtained for the Ω -profiles from panel (a) in the case of the finite-height and infinitely long cylinders. Note that the modifications of the flow profiles due to endcaps significantly reduce the critical Lu and Rm for the onset of MRI.

TABLE II. Critical values of (Lu, Rm) for the MRI onset for both the ideal and modified TC profiles.

μ	Ideal TC profile	Modified TC profile
0.35	(5.9, 16.2)	(1.5, 4.6)
0.5	(9.3, 30.3)	(3.6, 11.5)

caps in the presence of an axial magnetic field, enabling the onset of MRI in those experiments. Consistent with this result, we have also showed above that the modification of the angular velocity profile due to the endcap effects can lower the critical Lu and Rm for the MRI onset. Earlier experiments by the Princeton group on the hydrodynamical stability of the TC flow showed that the angular velocity of the flow at the mid-height is very close to an ideal TC profile due to an optimized splitting endcaps [20, 21], which, in turn, would exclude the onset of MRI at lower critical Lu and Rm . This implies that the applied axial field plays a crucial role not only in inducing MRI, but also in modifying the flow profile. Hence, the effects of a magnetic field and the conductivity of the endcaps on the TC flow dynamics and Stewartson layer instability should be investigated in more detail to better understand the nature of MRI onset in the recent Princeton experiments.

IV. CONCLUSIONS

In this paper, we conducted 2D axisymmetric hydrodynamic study of a TC flow in the presence of split endcaps of the cylinders relevant to DRESHDYN-MRI setup, covering wide ranges of Reynolds numbers Re and the ratio of cylinders' angular velocities μ . We investigated in detail the dynamics of high- Re flow in the Rayleigh-stable,

quasi-Keplerian rotation regime of the cylinders. We showed that the flow achieves a steady state for $Re \lesssim 10^4$ with poloidal Ekman circulations due to the endcaps penetrating deeper into the flow. In this case, the Ekman and Stewartson shear layers near the endcaps and hence the bulk flow are stable, having a stationary and regular spatial structure. As Re increases further, Ekman layer remains stable, whereas the Stewartson layer becomes more and more unstable, gets distorted and eventually develops turbulence at $Re \gtrsim 10^4$ – the regime which is of immediate relevance to MRI experiments. This turbulence is most intensive near the endcaps, but weakens away from the endcaps, reaching a relatively low level almost uniform in the bulk flow, still disrupting the overall poloidal circulations though. The mean angular velocity of the flow is also nearly uniform along the axial direction, Rayleigh-stable in the bulk flow (except for moderate turbulence near the endcaps) and the more deviates from the ideal TC flow profile for infinite cylinders, the larger is Re .

We characterized the structure and sizes of the Ekman and Stewartson layers as a function of Re and μ , which exhibit scaling laws with respect to these parameters, but with different exponents in the laminar (at lower Re) and turbulent (at higher Re) regimes. This difference in the scalings can be attributed to small-scale vortices shed near the turbulent tail of the unstable Stewartson layer at high Re , limiting its length. These vortices travel through the bulk flow and dissipate quickly. For the same Re , the flow becomes more stable for larger μ , due to the decreased velocity drop at the endcap slit.

These results can be important for the experimental studies of MRI, since they suggest that those experiments, which usually require higher $Re \gtrsim 10^6$ for the onset of MRI, could also be conducted at higher μ to exclude any hydrodynamic instability in the system interfering with MRI and complicating its dynamics and unambiguous identification. Furthermore, carrying out a preliminary linear stability analysis using the angular velocity profile in the considered TC setup with endcaps in the saturated state by introducing an axial magnetic field, we showed that such a modified flow profile results in the critical Lundquist Lu and magnetic Reynolds Rm numbers for MRI to set in about 3 times lower than those in the case of an ideal, infinitely long TC setup. This is another important result of this paper for the upcoming DRESHDYN-MRI experiment that in those experiments MRI can be in fact observed at much lower Lu and Rm than those dictated by the linear analysis for the ideal TC flow profile. All these questions, however, should be addressed in a systematic way in the full 3D MHD regime, including the behavior of Ekman and Stewartson layers, for the same finite-length TC setup subject to a background axial field. This will allow us to better understand the dynamics and evolution of MRI under the influence of endcaps in the given TC setup, thereby preparing a theoretical basis for the upcoming DRESHDYN-MRI experiment. The present hydrodynamic study is a first step

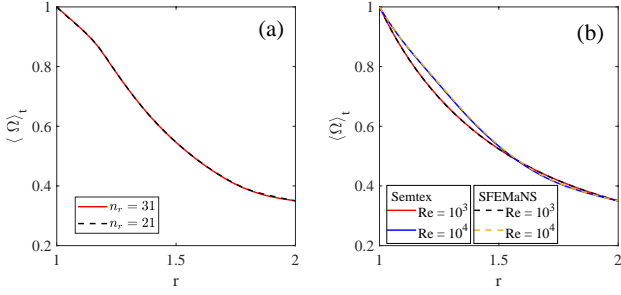


FIG. 12. (a) Time-averaged radial profile of the angular velocity, $\langle \Omega \rangle_t$, in the saturated state at mid-height for $Re = 2 \times 10^5$, $\mu = 0.35$ and $n_r = 21$ (black-dashed) and 31 (red), while $n_z = 201$ is fixed. (b) Comparison of, $\langle \Omega \rangle_t$, in the saturated state at mid-height obtained from SEMTEX and SFEMaNS codes for different Re .

forming the basis for such a more general MHD analysis.

ACKNOWLEDGMENTS

This work received funding from the European Union's Horizon 2020 research and innovation program under the ERC Advanced Grant Agreement No. 787544 and from Shota Rustaveli National Science Foundation of Georgia (SRNSFG) [grant number FR-23-1277]. PP was supported by the European Research Council (ERC) under the European Union's Horizon 2020 research and innovation program (grant agreement no. 847433, THEIA project).

DATA AVAILABILITY STATEMENT

Appendix A: Resolution and other case studies

To check the validity of our discretization approach, Fig. 12(a) shows the time-averaged angular velocity, $\langle \Omega \rangle_t$, at the mid-height as a function of r for $Re = 2 \times 10^5$ and $\mu = 0.35$ for two radial resolutions $n_r \in \{21, 31\}$. It is clearly seen that $n_r = 21$ can resolve the flow profile quite well even for $Re \leq 2 \times 10^5$.

To ensure the validity of our code, in Fig. 12(b) we further compare the flow profiles at the mid-height in the saturated state for $Re \in \{10^3, 10^4\}$ computed using two different codes: SEMTEX used in this paper and the Spectral/Finite Element code for Maxwell and Navier-Stokes Equations (SFEMaNS) [50, 51] extensively used for the simulations of the Princeton MRI-experiment [46, 48, 49, 52]. The finite element nature of SFEMaNS is well suited to model important fluid-boundary interactions in the experimental device. The code solves the Navier-Stokes and induction equations for incompressible flow on a mesh in the poloidal (r, z) -plane, divided into fluid, solid and vacuum domains. This comparison of the Ω -profiles demonstrates a very good agreement between

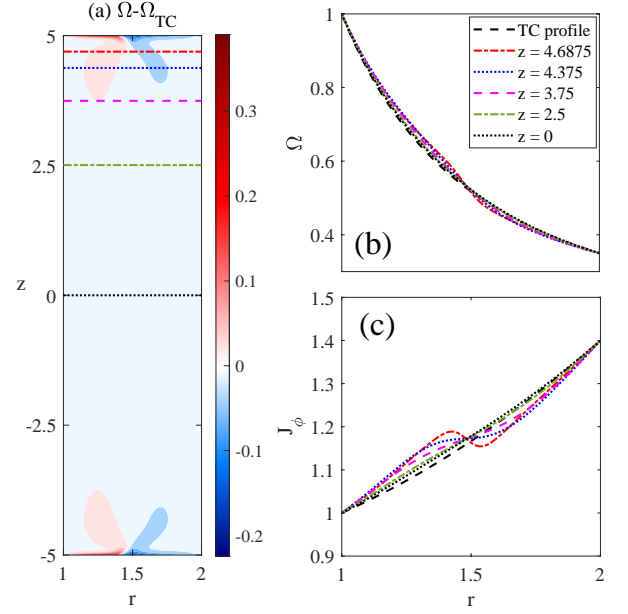


FIG. 13. (a) Deviation, $\Omega - \Omega_{TC}$, of the angular velocity Ω from Ω_{TC} in the (r, z) -plane and (b) the radial profile of Ω at different z [marked by horizontal lines in (a)] in the saturated state for $Re = 10^3$. (c) The specific angular momentum $J_z = r^2 \Omega$ vs. r at the same z as in (b).

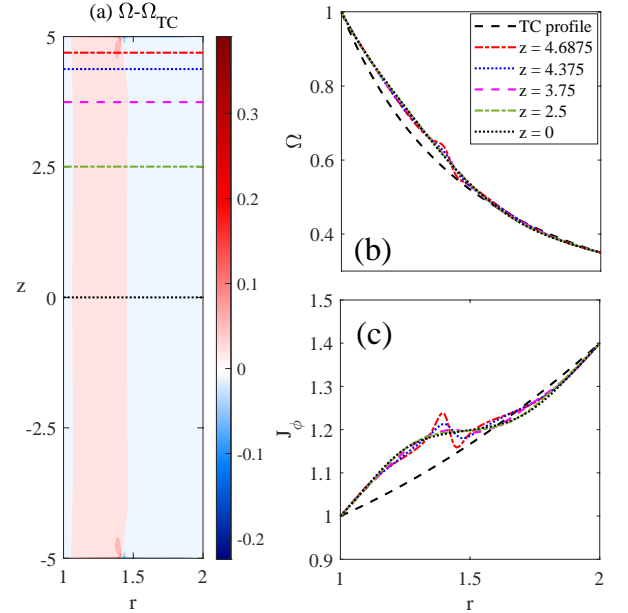


FIG. 14. Same as in Fig. 13 but for $Re = 10^4$.

these two codes.

Figure 13(a) shows the deviation, $\Omega - \Omega_{TC}$, of the flow angular velocity Ω from the ideal one Ω_{TC} in the (r, z) -plane as in Fig. 3 but for $Re = 10^3$. It is seen that this deviation is very small everywhere in the bulk flow except some perturbation near the slit r_s of the endcaps. The similarity between these two angular velocities is also confirmed in Fig. 13(b), showing the radial profile of Ω at

different z . Also, the azimuthal ϕ -component of angular momentum is closer to that of the ideal TC flow over the axial extent for this Re except a small deviation near the endcaps [Fig. 13(c)]. By contrast, at higher $Re = 10^4$ shown in Fig. 14(a), $\Omega - \Omega_{TC}$ is larger and nearly uniform

in z in the bulk flow. Fig. 14(b) shows that Ω is slightly larger than Ω_{TC} at $r \lesssim 1.5$ while following a nearly ideal TC profile at $r \gtrsim 1.5$. This deviation in the flow profile causes the angular momentum to increase near the inner part and slightly decrease in the outer part [Fig. 14(c)].

-
- [1] E. Velikhov, Stability of an ideally conducting liquid flowing between rotating cylinders in a magnetic field, *Zh. Eksp. Teor. Fiz.* **36**, 1398 (1959).
- [2] S. A. Balbus and J. F. Hawley, A Powerful Local Shear Instability in Weakly Magnetized Disks. I. Linear Analysis, *Astrophys. J.* **376**, 214 (1991).
- [3] H. Ji, M. Burin, E. Schartman, and J. Goodman, Hydrodynamic turbulence cannot transport angular momentum effectively in astrophysical disks, *Nat.* **444**, 343 (2006).
- [4] M. Avila, Stability and Angular-Momentum Transport of Fluid Flows between Corotating Cylinders, *Phys. Rev. Lett.* **108**, 124501 (2012).
- [5] J. M. Lopez and M. Avila, Boundary-layer turbulence in experiments on quasi-Keplerian flows, *J. Fluid Mech.* **817**, 21 (2017).
- [6] H. Ji and J. Goodman, Taylor-Couette flow for astrophysical purposes, *Philos. Trans. R. Soc. A* **381**, 20220119 (2023).
- [7] D. Feldmann, D. Borrero-Echeverry, M. J. Burin, K. Avila, and M. Avila, Routes to turbulence in Taylor-Couette flow, *Phil. Trans. R. Soc. A* **381**, 10.1098/rsta.2022.0114 (2023).
- [8] G. Rüdiger, M. Gellert, R. Hollerbach, M. Schultz, and F. Stefani, Stability and instability of hydromagnetic Taylor-Couette flows, *Phys. Rep.* **741**, 1 (2018).
- [9] A. Kageyama, H. Ji, J. Goodman, F. Chen, and E. Shoshan, Numerical and Experimental Investigation of Circulation in Short Cylinders, *J. Phys. Soc. Jpn.* **73**, 2424 (2004).
- [10] F. Stefani, G. Gerbeth, T. Gundrum, R. Hollerbach, J. Priede, G. Rüdiger, and J. Szklarski, Helical magnetorotational instability in a Taylor-Couette flow with strongly reduced Ekman pumping, *Phys. Rev. E* **80**, 066303 (2009).
- [11] J. Goodman and H. Ji, Magnetorotational instability of dissipative Couette flow, *J. Fluid Mech.* **462**, 365 (2002).
- [12] G. Rüdiger, M. Schultz, and D. Shalybkov, Linear magnetohydrodynamic Taylor-Couette instability for liquid sodium, *Phys. Rev. E* **67**, 046312 (2003).
- [13] A. Mishra, G. Mamatsashvili, and F. Stefani, From helical to standard magnetorotational instability: Predictions for upcoming liquid sodium experiments, *Phys. Rev. Fluids* **7**, 064802 (2022).
- [14] G. Rüdiger and M. Schultz, The gap-size influence on the excitation of magnetorotational instability in cylindrical Taylor-Couette flows, *J. Plasma Phys.* **90**, 905900105 (2024).
- [15] H. Ji, J. Goodman, and A. Kageyama, Magnetorotational instability in a rotating liquid metal annulus, *Mon. Not. R. Astron. Soc.* **325**, L1 (2001).
- [16] R. Hollerbach and A. Fournier, End-effects in rapidly rotating cylindrical Taylor-Couette flow, in *MHD Couette Flows: Experiments and Models*, American Institute of Physics Conference Series, Vol. 733, edited by R. Rosner, G. Rüdiger, and A. Bonanno (2004) pp. 114–121.
- [17] M. J. Burin, H. Ji, E. Schartman, R. Cutler, P. Heitzenroeder, W. Liu, L. Morris, and S. Raftopolous, Reduction of Ekman circulation within Taylor-Couette flow, *Exp. Fluids* **40**, 962 (2006).
- [18] E. Schartman, H. Ji, and M. J. Burin, Development of a Couette-Taylor flow device with active minimization of secondary circulation, *Rev. Sci. Instrum.* **80**, 024501-024501-8 (2009).
- [19] E. Schartman, H. Ji, M. J. Burin, and J. Goodman, Stability of quasi-Keplerian shear flow in a laboratory experiment, *Astron. Astrophys.* **543**, A94 (2012).
- [20] E. M. Edlund and H. Ji, Nonlinear stability of laboratory quasi-Keplerian flows, *Phys. Rev. E* **89**, 021004 (2014).
- [21] E. M. Edlund and H. Ji, Reynolds number scaling of the influence of boundary layers on the global behavior of laboratory quasi-Keplerian flows, *Phys. Rev. E* **92**, 043005 (2015).
- [22] L. Shi, B. Hof, M. Rampp, and M. Avila, Hydrodynamic turbulence in quasi-Keplerian rotating flows, *Phys. Fluids* **29**, 044107 (2017).
- [23] M. S. Paoletti and D. P. Lathrop, Angular Momentum Transport in Turbulent Flow between Independently Rotating Cylinders, *Phys. Rev. Lett.* **106**, 024501 (2011).
- [24] M. S. Paoletti, D. P. M. van Gils, B. Dubrulle, C. Sun, D. Lohse, and D. P. Lathrop, Angular momentum transport and turbulence in laboratory models of Keplerian flows, *Astron. Astrophys.* **547**, A64 (2012).
- [25] F. Nordsiek, S. G. Huisman, R. C. A. van der Veen, C. Sun, D. Lohse, and D. P. Lathrop, Azimuthal velocity profiles in Rayleigh-stable Taylor-Couette flow and implied axial angular momentum transport, *J. Fluid Mech.* **774**, 342 (2015).
- [26] F. Stefani, A. Gailitis, G. Gerbeth, A. Giesecke, T. Gundrum, G. Rüdiger, M. Seilmayer, and T. Vogt, The DRESHDYN project: liquid metal experiments on dynamo action and magnetorotational instability, *Geophys. Astrophys. Fluid Dyn.* **113**, 51 (2019).
- [27] G. Wendt, Potentialtheoretische Behandlung des Wehneltzylinders, *Ann. Phys.* **409**, 445 (1933).
- [28] D. Coles, Transition in circular Couette flow, *J. Fluid Mech.* **21**, 385 (1965).
- [29] D. Richard and J.-P. Zahn, Turbulence in differentially rotating flows. What can be learned from the Couette-Taylor experiment, *Astron. Astrophys.* **347**, 734 (1999).
- [30] J. Szklarski, Reduction of boundary effects in the spiral MRI experiment PROMISE, *Astron. Nachr.* **328**, 499 (2007).
- [31] C. Gissinger, J. Goodman, and H. Ji, The role of boundaries in the magnetorotational instability, *Phys. Fluids* **24**, 10.1063/1.4737657 (2012).
- [32] D. Choi, F. Ebrahimi, K. J. Caspary, E. P. Gilson, J. Goodman, and H. Ji, Nonaxisymmetric simulations of

- the Princeton magnetorotational instability experiment with insulating and conducting axial boundaries, *Phys. Rev. E* **100**, 033116 (2019).
- [33] H. M. Blackburn and S. J. Sherwin, Formulation of a Galerkin spectral element-Fourier method for three-dimensional incompressible flows in cylindrical geometries, *J. Comput. Phys.* **197**, 759 (2004).
- [34] H. M. Blackburn, D. Lee, T. Albrecht, and J. Singh, Semtex: A spectral element-Fourier solver for the incompressible Navier-Stokes equations in cylindrical or Cartesian coordinates, *Comput. Phys. Commun.* **245**, 106804 (2019).
- [35] A. Mishra, G. Mamatsashvili, and F. Stefani, Nonlinear evolution of magnetorotational instability in a magnetized Taylor-Couette flow: Scaling properties and relation to upcoming DRESHDYN-MRI experiment, *Phys. Rev. Fluids* **8**, 083902 (2023).
- [36] A. Mishra, G. Mamatsashvili, and F. Stefani, Nonaxisymmetric modes of magnetorotational and possible hydrodynamical instabilities in the upcoming DRESHDYN-MRI experiments: Linear and nonlinear dynamics, *Phys. Rev. Fluids* **9**, 033904 (2024).
- [37] Greenspan, *The Theory of Rotating Fluids* (Cambridge University Press, Cambridge, England, UK, 1968).
- [38] Since the flow is approximately symmetric around the mid-height $z = 0$, the radial profiles in the lower half of the cylinders are similar.
- [39] K. Stewartson, On almost rigid rotations, *J. Fluid Mech.* **3**, 17 (1957).
- [40] W. Liu, Magnetized Ekman layer and Stewartson layer in a magnetized Taylor-Couette flow, *Phys. Rev. E* **77**, 056314 (2008).
- [41] J. Szklarski and G. Rüdiger, Ekman-Hartmann layer in a magnetohydrodynamic Taylor-Couette flow, *Phys. Rev. E* **76**, 066308 (2007).
- [42] A. I. Vooren, The Stewartson layer of a rotating disk of finite radius, *J. Eng. Math.* **26**, 131 (1992).
- [43] The Ekman layer at the inner endcap rim remains nearly unchanged with μ , since only Ω_{out} is increased in μ .
- [44] A. Mishra, G. Mamatsashvili, V. Galindo, and F. Stefani, Convective, absolute and global azimuthal magnetorotational instabilities, *J. Fluid Mech.* **922**, R4 (2021).
- [45] A. Mishra, G. Mamatsashvili, M. Seilmayer, and F. Stefani, One-winged butterflies: mode selection for azimuthal magnetorotational instability by thermal convection, *J. Fluid Mech.* **992**, R1 (2024).
- [46] Y. Wang, F. Ebrahimi, H. Lu, J. Goodman, E. P. Gilson, and H. Ji, Observation of nonaxisymmetric standard magnetorotational instability induced by a free-shear layer, arXiv e-prints, arXiv:2411.02361 (2024).
- [47] The details of the eigenvalue problem, linear MHD equations and a pseudo-spectral code used to solve them are given in [13].
- [48] Y. Wang, E. P. Gilson, F. Ebrahimi, J. Goodman, and H. Ji, Observation of Axisymmetric Standard Magnetorotational Instability in the Laboratory, *Phys. Rev. Lett.* **129**, 115001 (2022).
- [49] Y. Wang, E. P. Gilson, F. Ebrahimi, J. Goodman, K. J. Caspary, H. W. Winarto, and H. Ji, Identification of a non-axisymmetric mode in laboratory experiments searching for standard magnetorotational instability, *Nat. Commun.* **13**, 4679 (2022).
- [50] J.-L. Guermond, R. Laguerre, J. Léorat, and C. Nore, Nonlinear magnetohydrodynamics in axisymmetric heterogeneous domains using a fourier/finite element technique and an interior penalty method, *J. Comput. Phys.* **228**, 2739 (2009).
- [51] C. Nore, D. C. Quiroz, L. Cappanera, and J.-L. Guermond, Direct numerical simulation of the axial dipolar dynamo in the von kármán sodium experiment, *EPL* **114**, 65002 (2016).
- [52] H. W. Winarto, H. Ji, J. Goodman, F. Ebrahimi, E. P. Gilson, and Y. Wang, Parameter space mapping of the Princeton magnetorotational instability experiment, *Phys. Rev. E* **102**, 023113 (2020).